J. Fluid Mech. (1982), *vol.* 118, *pp.* 269–284
Printed in Great Britain

An experimental investigation of oscillatory flow in pipe bends

By ARNOLD F. BERTELSEN AND LEIF K. THORSEN

Institute of Mathematics, Department of Mechanics,
University of Oslo, Norway

(Received 20 July 1981)

Oscillatory flow in U-shaped pipes has been investigated experimentally. The velocity field is mapped by observing the motion of tracer particles either photographically or by laser–Doppler anemometry. The most important result seems to be the observation of regions with strong secondary streaming at the inlet of the curved section, which, to the best of our knowledge, has not been reported before.

1. Introduction

Knowledge of the flow field in pipe bends with various inlet conditions is of importance both in engineering and physiology. U-shaped pipes of Plexiglas have been used in this investigation in order to study such flow fields for purely oscillatory laminar inlet flow (i.e. the flow in the straight pipes far from the bend). The purpose was to map the flow field at various stations of the pipe and to interpret the results in the light of earlier theoretical and experimental investigations. In this context the papers of Lyne (1970, 1971) and Mullin & Greated (1980) are of especial interest. The papers of Smith (1976) and Singh, Sinha & Aggarwal (1978) where pulsatile flow in pipe bends are studied, are also of some interest; unfortunately, however, these authors do not consider backflow of the axial component of the velocity.

The paper of Greated & Mullin is an experimental investigation of fully developed oscillatory laminar flow entering a curved pipe from a straight section. The investigation pays special attention to the alteration of the velocity profiles of the straight section to those of the curved pipe. We too have studied this alteration, but we put the main emphasis on the exploration of nonlinear streaming effects. This led us to the observation of strong secondary flows at the inlet of the bend, which to the best of our knowledge has not been reported before. The secondary streaming induced by oscillatory flow along a torus, described theoretically by Lyne (1970), has also been observed.

The most convenient theoretical model with respect to comparison with some of our experimental data seems to be that of Lyne (1970), which describes the velocity field induced in a torus by a uniform pressure gradient varying sinusoidally in time.

For later use we quote some of his results here. Using perturbation methods it is possible to write the axial component of the velocity field induced by the aforementioned pressure gradient as the following asymptotic expansion;

$$w = w_0(\eta,\tau) + \beta w_1(\eta,\tau) + \beta^2 w_2(\eta,\psi,\tau,R_s) + \delta w_{10}(\eta,\psi,\tau) + \delta\beta w_{11}(\eta,\psi,\tau) + \ldots, \quad (1)$$

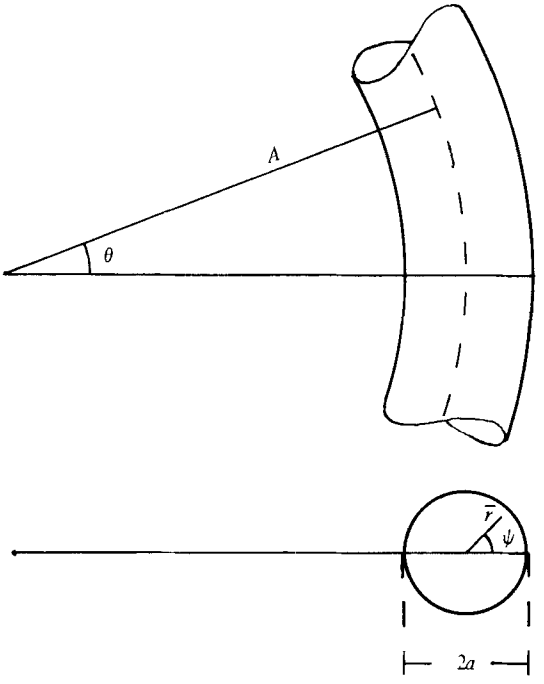

FIGURE 1. The co-ordinate system referred to in the text.

where w_0, w_1 and w_2 are given by equations (3.19), (3.36) and (3.50) in Lyne (1970), while Bertelsen (1974), using Lyne's expansion scheme, found

$$\left.\begin{aligned} w_{10} &= -[\sin\tau - e^{-\eta}\sin(\tau-\eta)]\cos\psi, \\ w_{11} &= \eta\cos\psi\sin\tau. \end{aligned}\right\} \tag{2}$$

The parameters β and δ, which appear in the dimensionless form of Navier–Stokes equations, are assumed to be small, and are defined as

$$\beta = \frac{1}{a}\left(\frac{2\nu}{\omega}\right)^{\frac{1}{2}} \ll 1, \quad \delta = \frac{a}{A} \ll 1, \tag{3}$$

where a is the radius of the pipe, ν the kinematic viscosity of the fluid, ω the circumferential frequency of oscillation and A the radius of the torus. The boundary-layer co-ordinate η is defined as

$$\eta = (1-r)/\beta, \tag{4}$$

where r is the dimensionless radial position $r = \bar{r}/a$ ($\bar{r}$ and ψ are radial and angular positions as indicated in figure 1).

The secondary steady streaming induced in the cross-section plane of the pipe can be depicted by a stream function $\chi(r,\psi;\beta;\delta;R_s)$. Lyne (1970) gave an approximate solution for χ, where, among other things, terms $O(\delta)$ were neglected. Including such terms, an uniformly valid expression of the stream function can be written:

$$\begin{aligned}\chi(r,\psi;\beta;\delta;R_s) &= \beta X_0^{(s)}(\eta,\psi)+\beta^2 X_1^{(s)}(\eta,\psi)+\beta\delta X_{01}^{(s)}(\eta,\psi)+\chi_{00}(r,\psi)+R_s\chi_{01}(r,\psi)\\ &+R_s^2\chi_{02}(r,\psi)+\beta R_s\chi_{11}(r,\psi)+\beta R_s^2\chi_{12}(r,\psi)+\beta^2\chi_{20}(r,\psi)+\beta^2 R_s\chi_{21}(r,\psi)+\delta[\chi_{001}(r,\psi)\\ &+\beta\chi_{101}(r,\psi)+R_s\chi_{011}(r,\psi)]-M(\eta,\psi;\beta;\delta;R_s). \end{aligned}\tag{5}$$

The functions involved here, except for terms $O(\delta)$ and $M(\eta, \psi; \beta; \delta; R_s)$, are given explicitly by Lyne (1970) as follows: $X_0^{(s)}$ and $X_1^{(s)}$ are the steady parts of X_0 and X_1, given respectively by equations (3.26) on p. 27 and (3.41) on p. 30 of Lyne; χ_{00}, χ_{01} and χ_{02} are given respectively by equations (4.4) on p. 36, (4.6) and (4.8) on p. 37; χ_{10}, χ_{11} and χ_{12} are given respectively by equations (4.14), (4.16) and (4.18) on p. 38; while χ_{20} and χ_{21} can be found from equation (4.20) on p. 39 as

$$\chi_2^{(s)} = \chi_{22} + R_s \chi_{21}. \tag{6}$$

The Reynolds number R_s is defined as

$$R_s = 2\epsilon^2/\beta^2,$$

where $\epsilon^2 = W_0^2/\omega^2 aA$, and W_0 is the amplitude of the basic axial oscillatory velocity component.

Bertelsen (1974) found

$$X_{01}^{(s)}(\eta, \psi) = [\tfrac{5}{8} + \tfrac{1}{4}\eta + \tfrac{1}{8} e^{-2\eta} + \tfrac{1}{2} e^{-\eta} (\sin\eta + \cos\eta)] \sin 2\psi, \tag{7}$$

$$\chi_{001} = \tfrac{1}{8}(r^2 - r^4) \sin 2\psi, \tag{8}$$

$$\chi_{101} = -\tfrac{1}{16}(41r^2 - 31r^4) \sin 2\psi, \tag{9}$$

$$\chi_{011} = \tfrac{1}{18432}(8r - 33r^3 + 42r^5 - 17r^7) \sin\psi + \tfrac{67}{61440}(r^3 - 2r^5 + r^7) \sin 3\psi, \tag{10}$$

$$\begin{aligned} M = {} & \beta(\tfrac{5}{8} - \tfrac{1}{4}\eta) \sin\psi + \beta^2(\tfrac{3}{16} + \tfrac{1}{2}\eta) \sin\psi \\ & + \beta^2(\tfrac{3}{8} \sin\psi - \tfrac{1}{768} R_s \sin 2\psi + \tfrac{1}{7372800} R_s^2 \sin\psi)\, \eta^2 \\ & + \beta\delta(-\tfrac{5}{8} + \tfrac{1}{4}\eta) \sin 2\psi. \end{aligned} \tag{11}$$

The stream function given by (5) above will serve as the basis of comparison with measured velocities in the middle-cross-section plane of the bend (i.e. cross-section 1 in figure 2). The time-averaged velocity $(\bar{u}, \bar{v})$ (physical dimensions) in this cross-section is given by

$$(\bar{u}, \bar{v}) = \frac{\epsilon^2 \omega a}{1 + \delta r \cos\psi} \left(\frac{1}{r} \frac{\partial \chi}{\partial \psi}, -\frac{\partial \chi}{\partial r} \right). \tag{12}$$

2. The experimental system

2.1. *The pipe system and the pumps*

The experiments described in this paper were performed in a pipe system of Plexiglas. The system consisted of a bend (180°) connected to two straight pipes by smooth junctures (A and B in figure 2). The bend is cut as a channel with circular cross-section (radius 1 cm) through a Plexiglas block by a milling machine. Two models have been used, model I with $\delta = \frac{1}{6}$ and model II with $\delta = \frac{1}{4}$. Two pumps were connected to straight pipes (see figure 2) and forced the fluid to oscillate with a frequency stability of approximately 1 %. The amplitude of the overharmonics of the motion of the pistons were 2 % or less relative to the amplitude of the basic frequency. An electro-optical device mounted on the pump generated a pulse train that was used to obtain phase-locked sampling of the velocity field in the pipe.

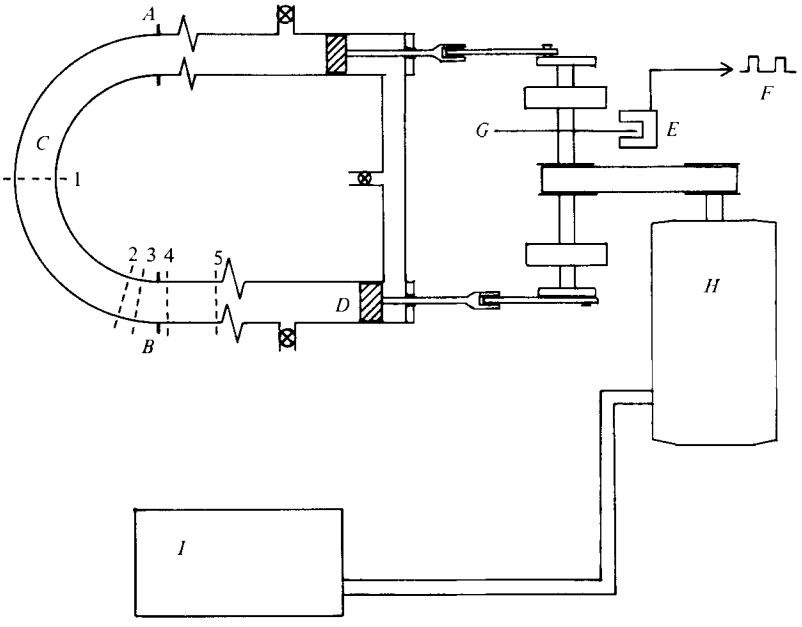

FIGURE 2. Main components of the pipe system and the pumps. A and B are the junctions of the bend C and the straight pipes D with the pistons. E is the electro-optical device, which generates a pulse train F when the disk G rotates. The electric motor H, supplied by the regulated power supply I, drives the pumps. The cross-sections 1, 2, 3, 4 and 5, referred to in the text, are also indicated.

2.2. *Method of observation and data acquisition*

The velocity field induced in the pipe system by the oscillating pistons was observed to some extent by photographic recording, but mainly by using a commercially available laser–Doppler anemometer (LDA), DISA 55 L, Mark II. Titanium oxide was added to the fluid in order to obtain sufficient scattered light for the LDA measurements. The optical components, including the laser and the photomultiplier, were mounted on a three-axis co-ordinate system, which could be moved to any position within its range and resolution by driving three step motors. Changes of position were controlled by a HP 9825A desk computer, which also served as controller of a HP 3052A Automatic Data Acquisition System equipped with the following main components: a scanner HP3437A, a multimeter HP3455A and a system voltmeter HP3437A (see figure 3). The multimeter was used to read the position indicators (potentiometers), while the system voltmeter sampled the output of the LDA. In order to measure the instantaneous velocity distribution across the pipe it was necessary to sample the velocity phase-locked relative to the pumps. This was achieved by utilizing the external triggering facility of the system voltmeter. The pulse train generated by the electro-optical device mentioned above passed some pulse-shaping electronics before it was fed to the 'external-triggering' input of the system voltmeter. The controller was programmed to let the external trigger initiate a sequence of typically ten samples during one period of the oscillatory motion of the fluid before the next external trigger pulse initiated a new sequence. The delay between each measurement in a sequence was controlled by the system voltmeter's own clock and was

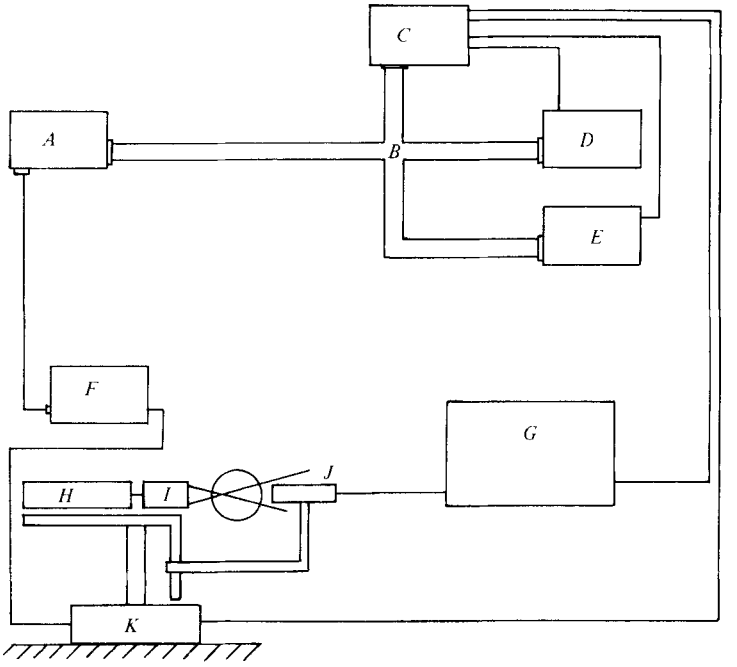

FIGURE 3. The main components of the laser–Doppler anemometer and the data-acquisition system. *A* indicates the controller HP9825A, *B* the interface bus, *C* the scanner HP3495A, *D* the multimeter HP3455A, *E* the system voltmeter HP3437A, *F* the BCD interface HP98032A, *G* the Doppler signal-processing equipment DISA 55L Mark II, *H* the laser, *I* the optical modulator, *J* the photomultiplier and *K* the step motors and position indicators.

chosen so that the time interval between the last measurement in a sequence and the first in the next sequence was equal to the delay itself. In this way several sequences gave a series of measurements all spaced equally in time. The velocity and position readings and other data of interest were fed to the controller and stored on magnetic tape.

The purpose of the photographic recording, mentioned above, was twofold. Firstly, the recordings gave information about the gross features of the secondary streaming (see figure 11). Secondly, steady streaming velocities measured on the basis of the pictures were compared with the corresponding LDA readings. The results obtained by these two methods were equivalent within the accuracy of the measurements (see figure 16).

The fluid layers recorded photographically were illuminated by a sheet of stroboscopic light with a repetition frequency equal to the frequency of the pumps. Aluminium powder was added to the fluid to render the motion visible.

2.3. *Data analysis and validation tests*

The velocity readings collected as described above were analysed using a fast Fourier transform routine supplied by Hewlett-Packard. The analysis proceeded as follows. Each sequence, say j, consisting of typically ten samples taken in one period of the oscillatory motion of the fluid, was analysed by the FFT routine, giving the Fourier coefficients

$$a_{0,j},\ a_{1,j},\ a_{2,j}\ \text{(cosine terms)};\quad b_{1,j},\ b_{2,j}\ \text{(sine terms)}.$$

Cross-section:	(1)	(2)	(3)	(4)	(5)
Model I	−94·25	−3·95	−1·64	1·32	42·11
Model II	−62·83	−2·04	−0·72	1·91	42·70

TABLE 1. s (mm)

A sufficient number N of sequences was used to get the standard deviations

$$\Delta a_i = \left[\frac{1}{N-1}\sum_{j=1}^{N}(a_{i,j}-a_i)^2\right]^{\frac{1}{2}} \quad (i = 0, 1, 2), \tag{13}$$

$$\Delta b_i = \left[\frac{1}{N-1}\sum_{j=1}^{N}(b_{i,j}-b_i)^2\right]^{\frac{1}{2}} \quad (i = 1, 2) \tag{14}$$

of the mean values

$$a_i = \frac{1}{N}\sum_{j=1}^{N} a_{i,j}, \tag{15}$$

$$b_i = \frac{1}{N}\sum_{j=1}^{N} b_{i,j} \tag{16}$$

below some chosen limits. The phase of the basic frequency was determined by putting

$$a_1 \cos\tau + b_1 \sin\tau = (a_1^2 + b_1^2)^{\frac{1}{2}} \sin(\tau + \phi), \tag{17}$$

giving

$$\phi = \arccos\left\{\frac{b_1}{(a_1^2+b_1^2)^{\frac{1}{2}}}\right\}. \tag{18}$$

2.4. *The working fluid*

In order to obtain LDA measurements close to the pipe walls and to have non-distorted photographic recordings from these regions, it was necessary to use a fluid with the same index of refraction as the Plexiglas. A mixture of approximately 74 % kerosene (Shellsol K) and 26 % (by volume) of a lubricating oil (Gravex 21, Shell) had this property. The refraction indices of the fluid and the Plexiglas were matched within 1 ‰. The kinematic viscosity of the fluid was approximately 0·164 cm²/s at 293 K and the temperature coefficient was 0·0086 cm²/s K.

3. Results and discussion

Measured velocities in five cross-sections around the pipe system will be presented here. The cross-sections were located as indicated in table 1, where s is the distance from the juncture of the bend and straight pipe to the cross-section in question (the distance being measured along the axis of the pipe and reckoned positive into the straight section, see figure 2).

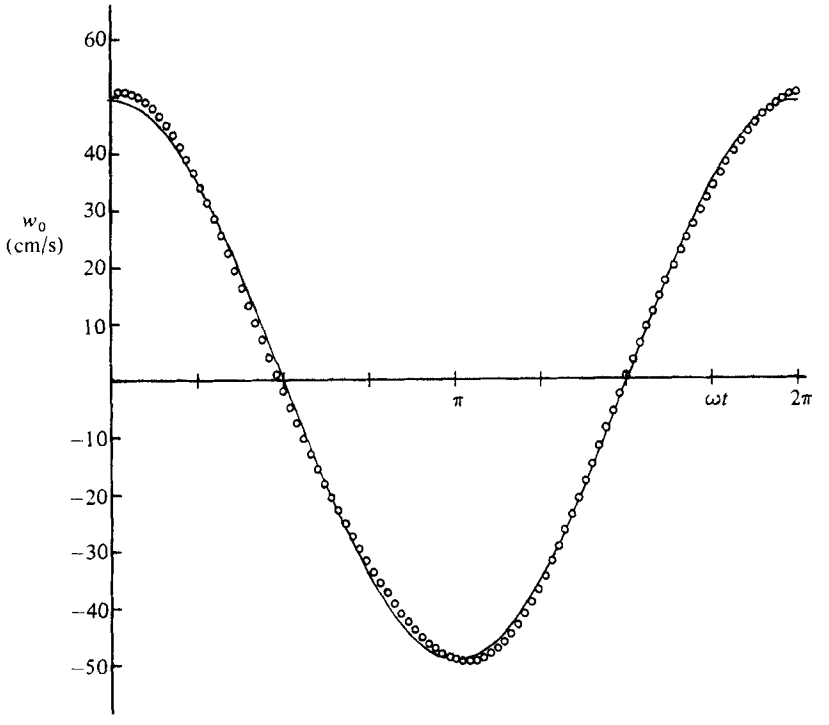

FIGURE 4. The basic flow w_0 at cross-section 5 ($r = 0$) as a function of time. Continuous curve is simple harmonic motion with frequency 12 Hz; circles indicate measured values.

3.1. *The inlet flow conditions*

On the basis of the construction of the pumps we could not expect pure simple-harmonic motion of the fluid in the straight section of the pipe. Therefore the inlet flow conditions were investigated experimentally by measuring the time evolution of the axial velocity component in cross-section 5 ($r = 0$) during several hundred periods of the piston motion. The measured velocities are plotted in figure 4, where a simple-harmonic motion is also indicated. The experimental values are average values of the velocity measured at a fixed phase in each period. The figure indicates that the inlet flow is sufficiently close to simple-harmonic motion that it will make sense to attribute expected nonlinear effects in the bend to self-interaction of the motion with the basic frequency.

The axial-velocity profile along a diameter in cross-section 5 has been investigated experimentally. On the basis of these measurements the variation of the phase along the diameter was calculated. The results are plotted in figure 5, where a theoretical curve based on (1) with $\delta = R_s = 0$ is also indicated. The theoretical curve is known to be a good approximation to the real phase variation. We therefore interpret the results presented in figure 5 as implying that the method of observation, including the phase-locked sampling of the LDA output, worked satisfactorily.

3.2. *The axial time-dependent component of the velocity*

The axial component of the velocity field was measured at 5 cross-sections along the pipe. Figures 6 and 7 show the measured values against radial position in models I

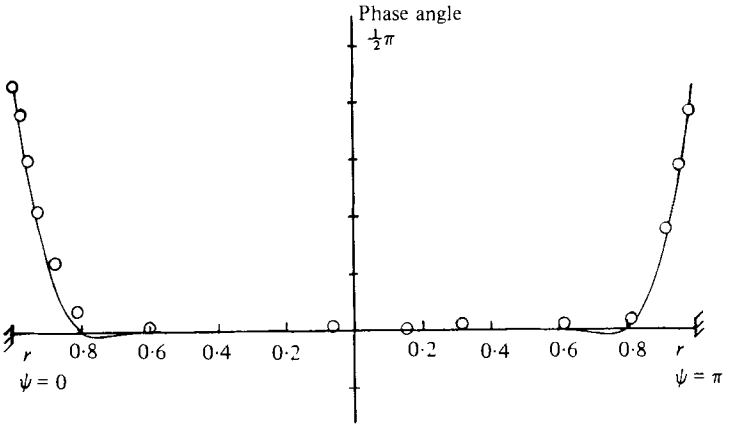

FIGURE 5. The phase variation along a diameter. The continuous curve is based on (1) ($\delta = R_s = 0$); circles indicate measured values.

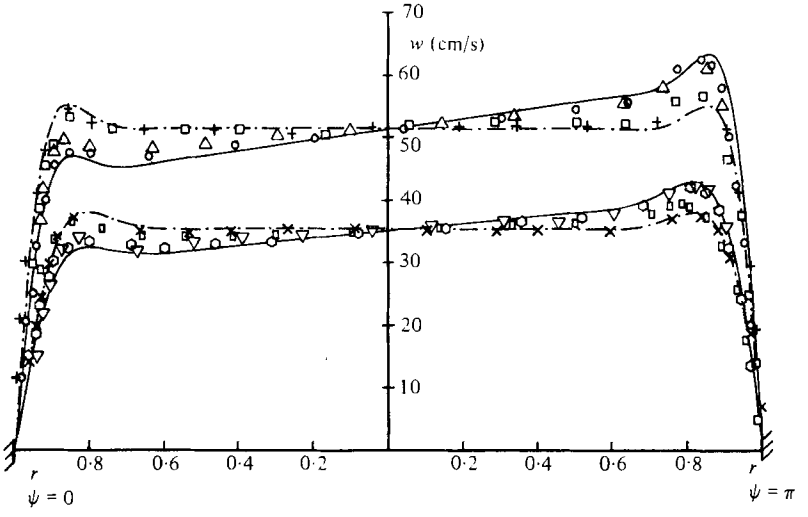

FIGURE 6. The profile of the unsteady, axial component of the velocity along a diameter in model I. The curves are based on (1). The upper continuous curve is for $f = 12$ Hz, $\beta = 0{\cdot}063$, $\delta = \frac{1}{6}$, $R_s = 39{\cdot}0$. The lower continuous curve is for $f = 9$ Hz, $\beta = 0{\cdot}080$, $\delta = \frac{1}{6}$, $R_s = 20{\cdot}4$. The corresponding broken curves have the same parameter values except for $\delta = R_s = 0$. The corresponding measured velocities at some points are also plotted. ○, △, □ and + indicate measurements for $f = 12$ Hz in cross-sections 2, 3, 4 and 5, respectively. ⬡, ▽, ▯ and × indicate measurements for $f = 9$ Hz in cross-sections 2, 3, 4 and 5 respectively.

and II. There is (to our knowledge) no theoretical model that describes the alteration of the velocity profiles in a straight pipe to those in the bend. Therefore theoretical profiles in a straight pipe and in a torus, based on (1) (in the straight pipe, $\delta = R_s = 0$), only could be drawn in the aforementioned figures. The amplitudes of theoretical and measured values of the velocity were put equal at $r = 0$. The measured velocities are the instantaneous values corresponding to $\tau = \frac{1}{2}\pi$ in (17), where $\tau = 0$ was chosen so that $\phi(r = 0) = 0$. A main feature of the experimental results presented in figures 6 and 7 is the gradual alteration of the constant velocity outside the Stokes layer in the straight pipe to the skew distribution in the bend. The skewness is caused essentially

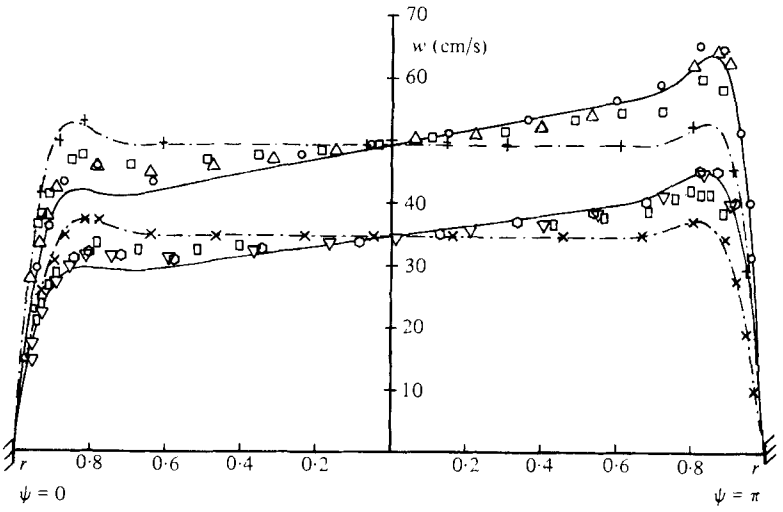

FIGURE 7. The profile of the unsteady, axial component of the velocity along a diameter in model II. The curves are based on (1). The upper continuous curve is for $f = 12$ Hz, $\beta = 0{\cdot}065$, $\delta = \frac{1}{4}$, $R_s = 50{\cdot}0$. The lower continuous curve is for $f = 9$ Hz, $\beta = 0{\cdot}079$, $\delta = \frac{1}{4}$, $R_s = 29{\cdot}8$. The corresponding broken curves have the same parameter values, except for $\delta = R_s = 0$. The measured velocities at some points are also plotted. ○, △, □, +, measurements for $f = 12$ Hz in cross-sections 2, 3, 4 and 5, respectively. ○, ▽, ▯, ×, measurements for $f = 9$ Hz in cross-sections 2, 3, 4 and 5 respectively.

by a higher pressure gradient along the inside ($\psi = \pi$) of the bend than along the outside ($\psi = 0$). On the basis of figures 6 and 7 we conclude that this skewness is established over a distance a (pipe radius) along the pipe. This is also expected on the basis of order-of-magnitude arguments. The length scale is expected to be determined by the potential flow outside the Stokes layer. The governing length scale in the potential flow around a body is usually a characteristic dimension of the body, in this case the radius of the pipe, and consequently independent of the amplitude. For sufficiently large values of $\delta\epsilon^2$ the secondary flow is expected to cause a further modification of the skew profiles discussed above.

Our results are a considerable supplement to those of Mullin & Greated (1980) which showed fully developed torus flow at $s \simeq -A$. In their experiments, however, the β-values were $0{\cdot}3 \leqslant \beta \leqslant 1{\cdot}4$, and the amplitude $\epsilon = O(1)$. For such parameter values, viscous effects are important in the core of the pipe also, and secondary-flow effects are the predominant mechanism causing modification of the inlet profile.

We also attempted to measure the first harmonic of the basic frequency. However, it turned out to be very difficult to get the error bounds of a_2 and b_2 sufficiently small to obtain meaningful results. (These problems could be due to elasticity and photoelasticity in the Plexiglas models.) Therefore, no measurements of a_2 and b_2 are discussed here.

3.3. *The secondary steady streaming*

The steady secondary streaming is difficult to measure in our case as it is heavily modulated by a large-amplitude oscillatory flow. The axial component is most difficult to observe, as the tracker then has to be set to a high range (large velocities) in order to keep tracking throughout the whole period of oscillation. Typically the tracker was

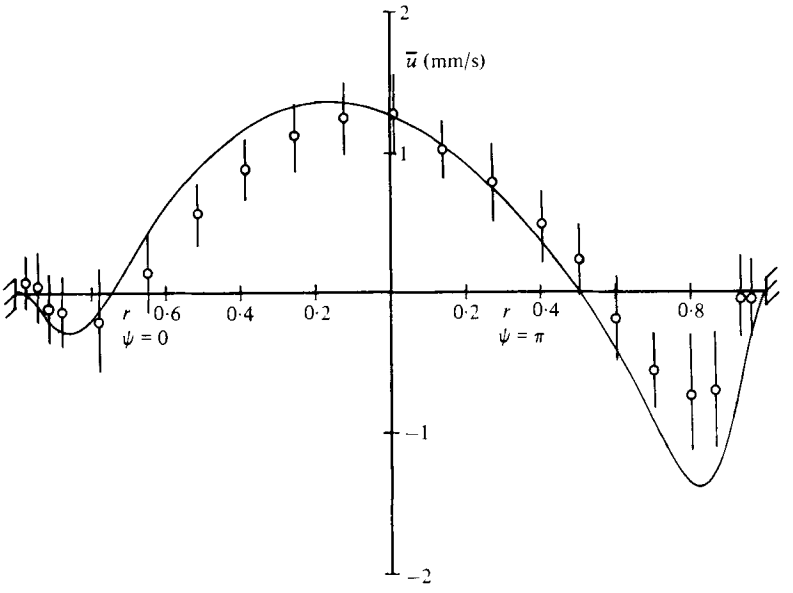

FIGURE 8. The time-averaged radial velocity $\bar{u}$ along a diameter in cross-section 1 in model I. The parameters have the same values as given for the measurements with 9 Hz in figure 6. The continuous curve is based on (5). ○, LDA measurements. The velocity is reckoned positive towards the centre of curvature of the bend.

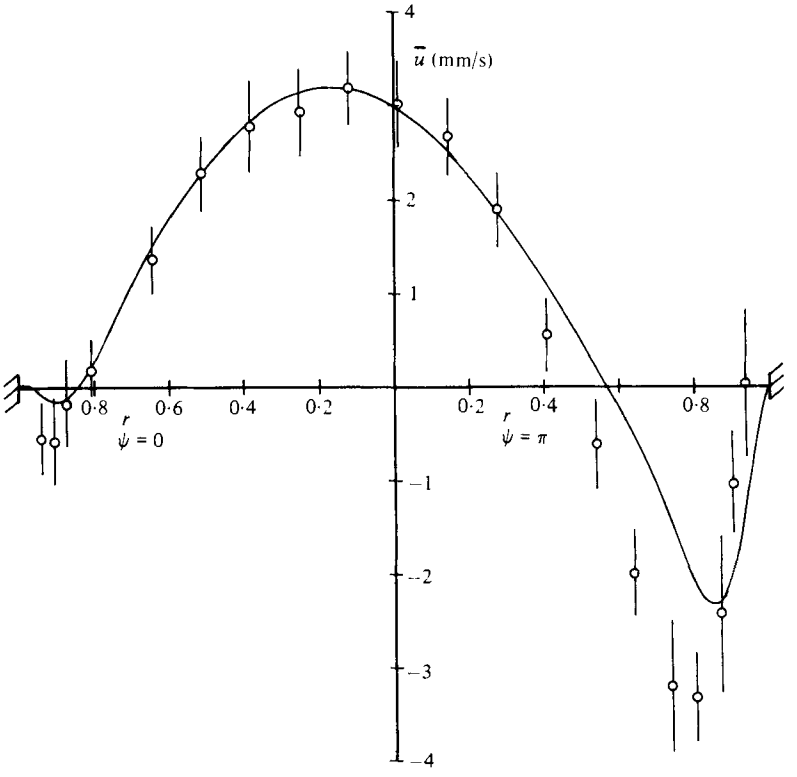

FIGURE 9. The time-averaged radial velocity $\bar{u}$ along a diameter in cross-section 1 in model II. The parameters have the same values as given for the measurements with 12 Hz in figure 7. The continuous curve is based on (5). ○, LDA measurements.

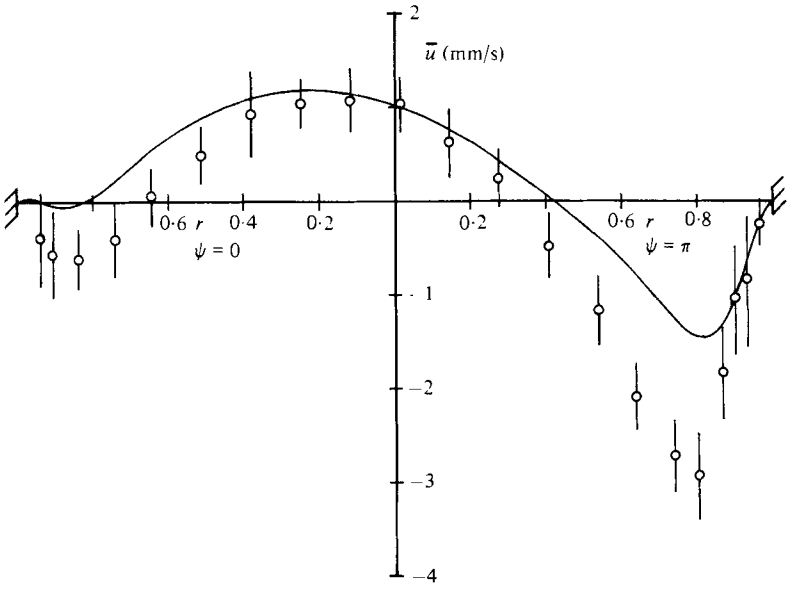

FIGURE 10. The time-averaged radial velocity $\bar{u}$ along a diameter in cross-section 1 in model II. The parameters have the same values as given for the measurements with 9 Hz in figure 7. The continuous curve is based on (5). ○, LDA measurements.

operated in velocity ranges of 2·8 m/s and 9·5 m/s (and a bandwidth of 2 % to give sufficient high slew rates of the tracking filter), while the secondary streaming is less than 2 cm/s. It turned out to be necessary to carry out a DC-offset calibration of the LDA at the various ranges in order to get reasonable velocity distributions of the secondary streaming. The calibration was achieved by observing the output of the LDA with the probe volume in a quiescent fluid.

In order to test the method of observation, the secondary streaming in cross-section 1 was measured. In this region of the bend, we expect Lyne's model (with additional terms, given by (5), due to the finite aspect ratio δ) to be a good approximation to the real flow field for $R_s \leqslant 30$ (see Kuwahara & Imai 1969). This theoretical model is compared with measured velocities in figures 8, 9 and 10. We believe that the good agreement between theoretical and measured velocities in these figures imply that the method of observation worked satisfactorily, also with respect to revealing secondary flows. In assessing the discrepancy between theory and experiment in figures 8, 9 and 10 it should be remembered that δ is not very small and $30 \leqslant R_s \leqslant 50$. Other regions in the pipe system susceptible to nonlinear streaming effects are the regions around the junctions of the straight pipes and the bend. The gross features of the secondary streaming in these regions are shown in figure 11, which is drawn on the basis of several photographs of a fluid layer in the axial plane of the U-shaped pipe. Such photographs together with direct visual observation indicate that there is a Stokes layer at the walls where the Reynolds stresses induce a steady velocity, which by viscous action forces the fluid in the core of the pipe to recirculate in an 'egg-formed' region. More detailed information on this secondary streaming is given in figures 12, 13 and 14, where the axial components of the secondary streaming at different cross-sections are plotted. There appears to be no essential difference between

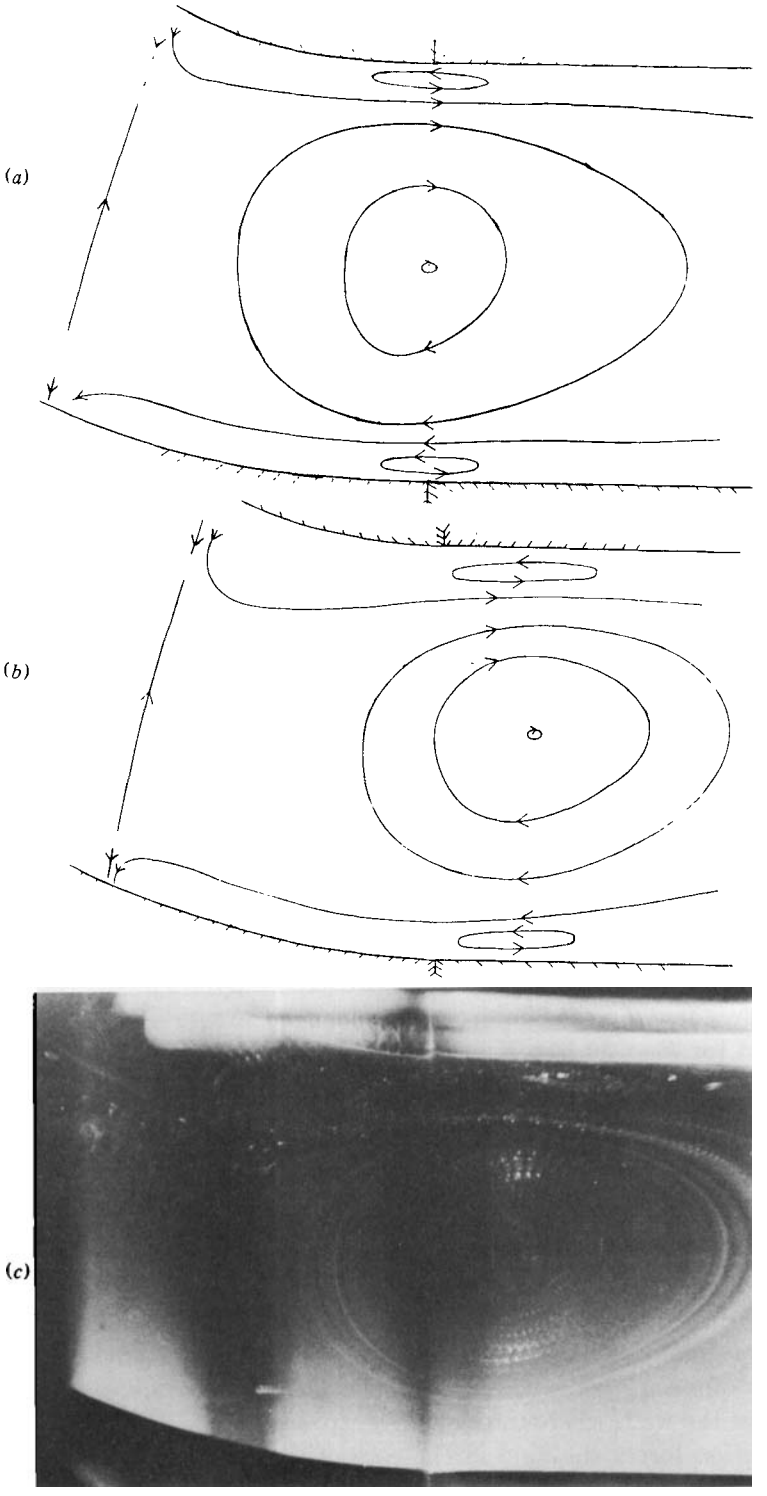

FIGURE 11. The streamline diagrams (*a*) and (*b*) indicate the main features of the secondary flow in the axial plane of the pipe system at the junction of the straight pipe and the bend. The diagrams are drawn on the basis of several photographs similar to (*c*), which corresponds to (*b*). The diagrams (*a*) and (*b*) depict the flow in models I and II respectively, both with frequency $f = 9$ Hz.

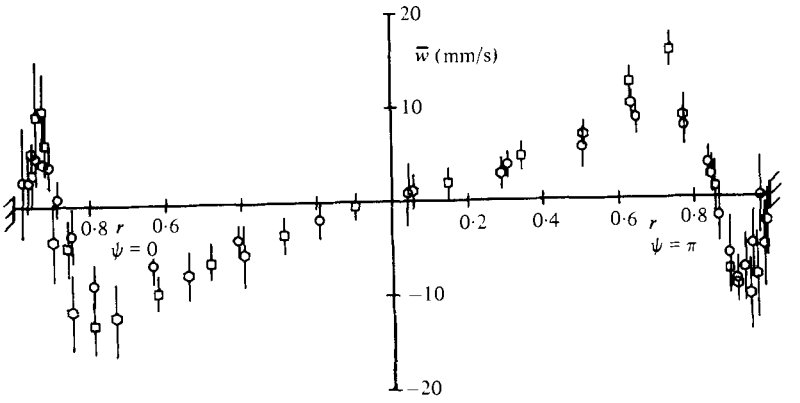

FIGURE 12. The measured time-averaged axial velocity component $\bar{w}$ in model I with frequency $f = 12$ Hz (for other parameters see figure 6). ○, □, ◇, LDA measurements in cross-sections 2, 3 and 4 respectively.

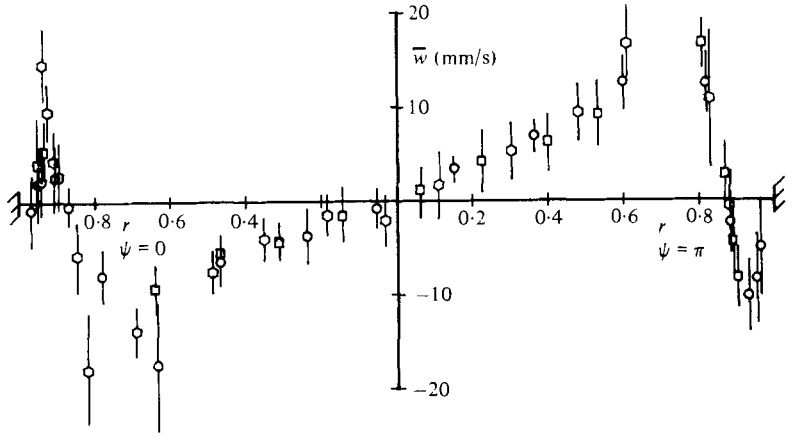

FIGURE 13. The measured time-averaged axial velocity component $\bar{w}$ in model II with frequency $f = 12$ Hz (for other parameters see figure 7). ○, □, ◇, LDA measurements in cross-sections 2, 3 and 4 respectively.

figures 12 and 13, where data from models I and II, both with frequency $f = 12$ Hz, are presented. The maximum streaming velocity seems to be a little higher in figure 13. This difference is expected since the most important generating terms of the secondary streaming are probably the time-averaged Reynolds stresses

$$\rho\left(\overline{u\frac{\partial w}{\partial r} + w\frac{\partial w}{\partial s}}\right).$$

The same difference is true for figure 14, where $f = 9$ Hz.

In figures 15 and 16 measured values of the radial component of the secondary flow at cross-section 4 are presented. These figures too indicate that the main features of the secondary streaming (except for the amplitude) are weakly dependent on the frequency when $\beta \ll 1$. The most striking feature of figures 15 and 16 is the change of sign of radial velocity when δ decreases from $\frac{1}{4}$ to $\frac{1}{6}$. This effect can most easily be observed in the streamline diagram of figure 11, from which it is clear that the core of the recirculating region is being displaced owing to finite δ-values.

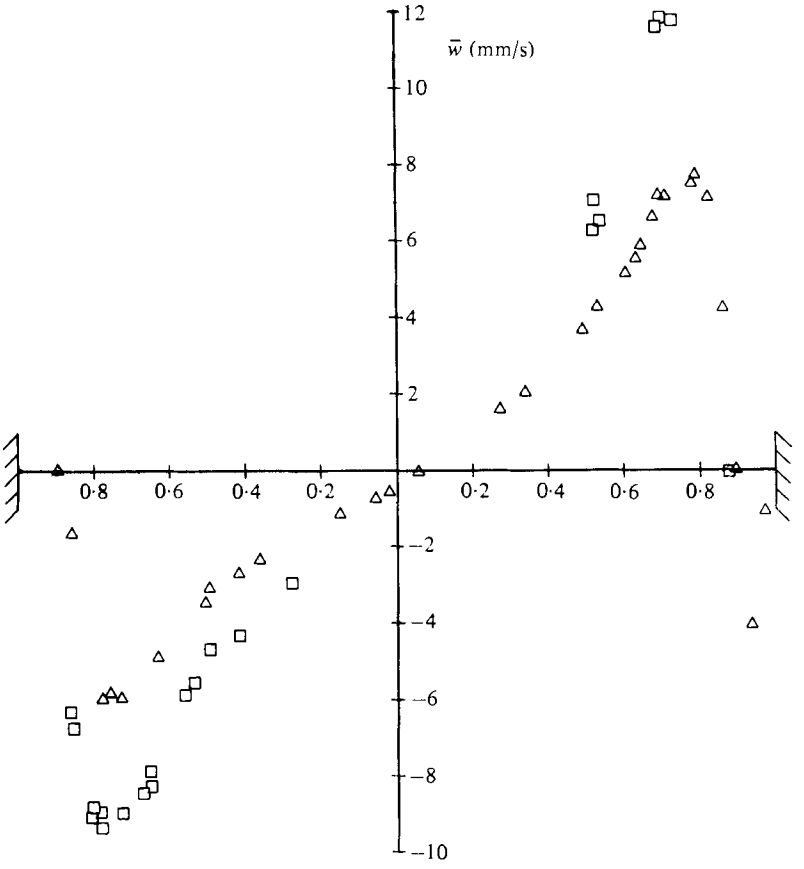

FIGURE 14. The measured time-averaged axial velocity component $\bar{w}$ in model I and II, both with frequency f = 9 Hz and in cross-section 4 (for other parameters, see figures 6 and 7 respectively). △ and □, measurements in models I and II respectively, based on photographic recordings.

4. Conclusions

An important conclusion that can be drawn from the results presented here is that essentially fully developed oscillating flow in a straight pipe and in a bend apply at positions $O(a)$ from the juncture of two such pipe components, assuming the Stokes layer to be thin compared with the radius of the pipe and assuming the amplitude to be moderate ($\epsilon < 1$). On the other hand, if the Stokes-layer thickness is of the order of the pipe radius, and the amplitude $\epsilon = O(1)$, then the results of Greated & Mullin (1980) should apply. They found fully developed flow in the bend at positions $O(A)$ from the inlet. The theoretical investigations of Smith (1976) and Singh *et al.* (1978) do not allow backflow; but, to the extent that any comparison with these results can be made, they are in accordance with our experiments. For example, Smith (1976) found both an upstream and a downstream inlet effect in a pipe model similar to that used here.

Finally, the most important result is probably the demonstration of the secondary streaming in the region at the junction of the straight pipe and the bend. A corres-

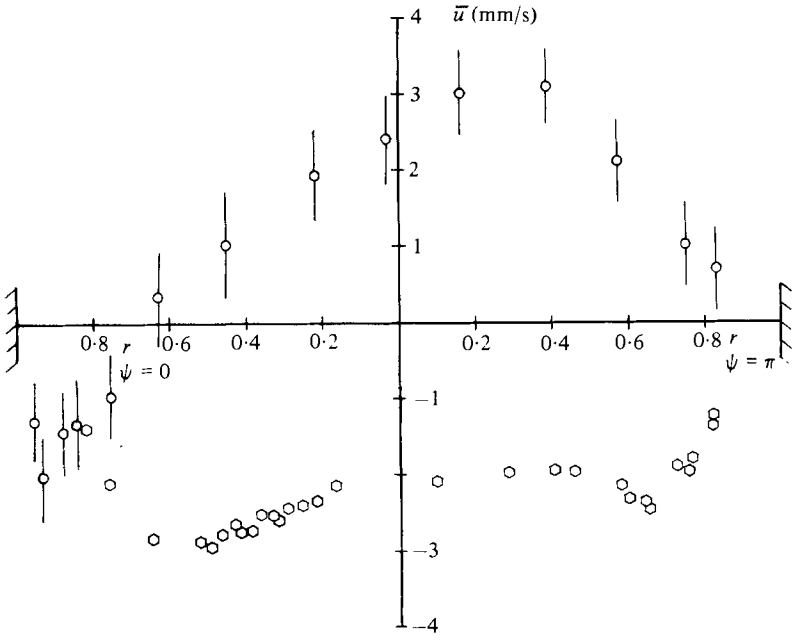

FIGURE 15. The measured time-averaged radial velocity component $\bar{u}$ in models I and II, both with frequency $f = 12$ Hz and in cross-section 4 (for other parameters, see figures 6 and 7 respectively). ○, ○, measurements in models I (photo) and II (LDA) respectively.

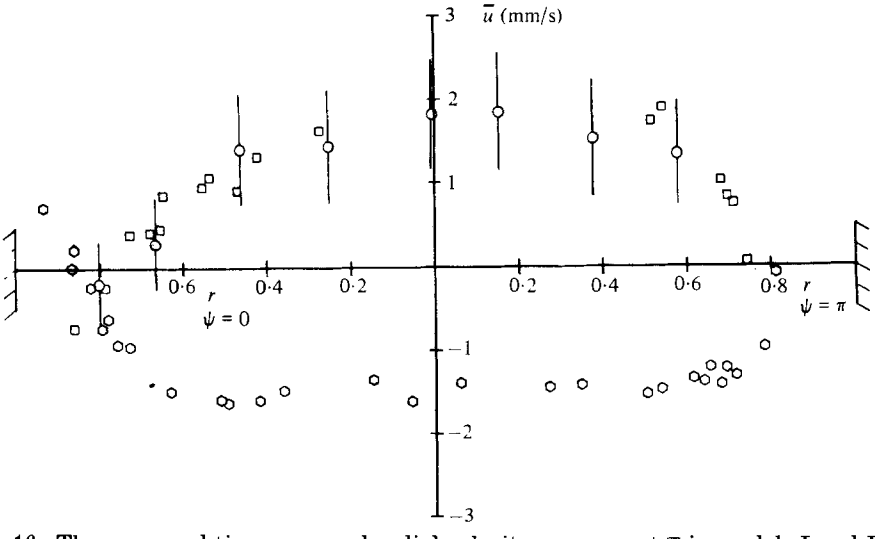

FIGURE 16. The measured time-averaged radial velocity component $\bar{u}$ in models I and II, both with frequency $f = 9$ Hz and in cross-section 4 (for other parameters, see figures 6 and 7 respectively). ○, □, measurements (photo) in models I and II respectively; ○, LDA measurements in model II.

ponding nonlinear effect will probably persist in a pulsating (non-zero mean) basic flow, but this problem is left for later investigations.

From an experimental point of view it is of some interest that it was possible to detect secondary flow around the inlet of the bend where this flow is heavily modulated

by the basic flow. The error bounds of the LDA measurements are large, but they can probably be improved by more sophisticated sampling techniques and more patience from the experimentalist.

REFERENCES

BERTELSEN, A. F. 1974 *Dept of Physics, University of Bergen, Rep.* no. 67.
KUWAHARA, K. & IMAI, J. 1969 *Phys. Fluids Suppl.* **12**, II94–101.
LYNE, W. H. 1970 Ph.D. thesis, University of London.
LYNE, W. H. 1971 *J. Fluid Mech.* **45**, 13–31.
MULLIN, T. & GREATED, C. A. 1980 *J. Fluid Mech.* **98**, 383–396.
SINGH, M. P., SINHA, P. C. & AGGARWAL, M. 1978 *J. Fluid Mech.* **87**, 97–120.
SMITH, F. T. 1976 *Proc. R. Soc. Lond.* A **351**, 71–87.